Biermann-Battery-Mediated Magnetic Reconnection in 3D Colliding Plasmas

J. Matteucci,[1,*] W. Fox,[1,2] A. Bhattacharjee,[1,2] D. B. Schaeffer,[1] C. Moissard,[3]
K. Germaschewski,[4] G. Fiksel,[5] and S. X. Hu[6]

[1]*Department of Astrophysical Sciences, Princeton University, Princeton, New Jersey 08540, USA*
[2]*Princeton Plasma Physics Laboratory, Princeton, New Jersey 08543, USA*
[3]*Laboratoire de Physique des Plasmas, École Polytechnique, Paris 75252, France*
[4]*Space Science Center, University of New Hampshire, Durham, New Hampshire 03824, USA*
[5]*Center for Ultrafast Optical Science, University of Michigan, Ann Arbor, Michigan 48109, USA*
[6]*Laboratory for Laser Energetics, University of Rochester, Rochester, New York 14623, USA*

Recent experiments have demonstrated magnetic reconnection between colliding plasma plumes, where the reconnecting magnetic fields were self-generated in the plasma by the Biermann-battery effect. Using fully kinetic 3D simulations, we show the full evolution of the magnetic fields and plasma in these experiments, including self-consistent magnetic field generation about the expanding plume. The collision of the two plasmas drives the formation of a current sheet, where reconnection occurs in a strongly time- and space-dependent manner, demonstrating a new 3D reconnection mechanism. Specifically, we observe a fast, vertically localized Biermann-mediated reconnection, an inherently 3D process where the temperature profile in the current sheet coupled with the out-of-plane ablation density profile conspires to break inflowing field lines, reconnecting the field downstream. Fast reconnection is sustained by both the Biermann effect and the traceless electron pressure tensor, where the development of plasmoids appears to modulate the contribution of the latter. We present a simple and general formulation to consider the relevance of Biermann-mediated reconnection in general astrophysical scenarios.

The Biermann-battery effect [1,2] is one of the few mechanisms known to spontaneously generate magnetic fields in plasmas. In the context of astrophysics, while too weak to generate the present-day observed cosmic magnetic fields, the Biermann-battery effect is widely regarded as a possible source of the seed magnetic field, subsequently amplified to observed present-day fields by protogalactic turbulence [2]. This effect, which is the result of noncollinearity between density and temperature gradients ($(\partial \boldsymbol{B}/\partial t) \propto \nabla n \times \nabla T$), has been shown in high-energy-density (HED) plasmas to generate strong magnetic fields (10–100 T) during intense laser heating [3–10]. In such experiments [3–5,10], when two plumes are ablated adjacently, the oppositely polarized fields collide and undergo magnetic reconnection; this is the universal process in which the magnetic field threaded through plasma undergoes a fundamental topological change, often resulting in violent conversions of field energy into kinetic energy. HED laser plasmas provide a platform to study magnetic reconnection, which is intrinsic to many phenomena throughout plasma physics [11], from the sawtooth instability in magnetic fusion confinement devices [12] to solar flares [13] and disturbances in Earth's magnetosphere [14].

Recent HED experiments have observed interesting effects associated with reconnection, including flux annihilation [4,15], stagnation of reconnection [10], and particle jets [3,7]. Kinetic simulations of HED laser experiments based on model profiles have provided valuable insight into reconnection dynamics in this regime, including flux-pileup near the reconnection layer [16], plasmoid formation [17], the role of the Nernst effect [18], and particle acceleration by reconnection [19]. Particle-in-cell simulations have also modeled Biermann-battery generation in expanding plasmas [20]. One such study investigated reconnection in electron-dominated relativistic plasmas driven by short-pulse lasers [21], but, to date, the full 3D evolution of magnetic reconnection within HED plasmas in the magnetohydrodynamic (MHD) regime ($L/d_i \gg 1$, where L is the system size and d_i is the ion skin depth) has not been investigated.

In this Letter, we present the first 3D, end-to-end, fully kinetic computational study of magnetic reconnection within a recent HED experiment [6], which captures both the *self-consistent* initial field generation by the Biermann effect and reconnection within the fully 3D geometry of the system. This is in contrast to previous HED reconnection simulations where the magnetic fields and plasma profiles are set in the initial conditions. We present in detail how reconnection proceeds, including how the development and ejection of plasmoids modulates the reconnection rate. The simulations also reveal that the Biermann-battery effect can play a direct and significant role in 3D magnetic reconnection, where a local T_e maximum in the current sheet

coupled with an out-of-plane density gradient conspires to reconnect flux via $\nabla n \times \nabla T$, a process we refer to as "Biermann-mediated reconnection." We emphasize that observing this mechanism requires a full 3D simulation, and it is distinct from previously documented 2D reconnection mechanisms, both in the strong guide-field case involving the electron scalar pressure [22,23] and in reconnection without a guide field involving the off-diagonal components of the electron pressure tensor [16,24]. We introduce a new dimensionless number that enables the evaluation of the importance of the Biermann effect in reconnection and demonstrate its application to laboratory and space plasmas.

For direct comparison, presented simulations are modeled after a recent reconnection experiment at the Shenguang-II (SG-II) laser facilities [6], for which we observe general agreement between the field and plasma evolution in simulation and experiment. The results of our simulation have potentially important implications for reconnection and energy conversion in many 3D reconnection systems. For example, in galactic dynamo theories where Biermann fields provide the seed magnetic field, it is implicitly assumed that fast reconnection occurs somehow to facilitate the breaking and reconfiguration needed to form large-scale magnetic fields [2]. Our Letter demonstrates that, in addition to seed generation, the Biermann effect might also facilitate the reconnection required for the success of a large-scale dynamo. Furthermore, this Letter is especially relevant to systems with large density and temperature gradients, such as in indirect and direct-drive inertial confinement fusion experiments [25,26] and reconnection in many astrophysical scenarios, including in Earth's magnetosheath [27], the heliopause [28], and in simulations of turbulent reconnection, including the highly turbulent reconnection upstream of high-Mach-number shocks [29].

We use the following formulation of generalized Ohm's law in order to quantitatively account for the contributions to the electric field, which in turn accounts for B-field evolution via Faraday's law,

$$E = -v \times B + \frac{j \times B}{n_e e} - \frac{\nabla p_e}{n_e e} - \frac{\nabla \cdot \Pi_e}{n_e e} + \frac{R_{ei}}{n_e e}. \quad (1)$$

Each term on the rhs has a physical interpretation; the first two terms are the contribution due to ion flow and the Hall effect. The third term represents the contribution due to the scalar electron pressure. Via Faraday's law, this term contributes to $(\partial B/\partial t)$ as the Biermann-battery effect, $-(1/n_e e)\nabla n_e \times \nabla T_e$, and is capable of generating or destroying magnetic flux depending on temperature, density, and field configurations. The fourth term, the traceless pressure tensor contribution (where $\Pi_e \equiv P_e - p_e I_3$) is well documented to be important in collisionless 2D reconnection layers [24]. This term includes the effect of viscosity and contributions from pressure tensor anisotropy, which is associated with the Weibel instability [30]. R_{ei} is the collisional momentum transfer between electrons and ions and via Faraday's law contributes to $(\partial B/\partial t)$ as both resistive diffusion and Nernst advection via the thermal force. Noting that reconnection is characterized by a finite out-of-plane E field inside the current sheet, we use Eq. (1) to quantify the contribution to the reconnection electric field from the Biermann-battery effect, which requires out-of-plane variation, and from the traceless pressure tensor term [24].

Simulation setup.—We use the PSC code [31], a fully kinetic, explicit particle-in-cell code employing a binary Coulomb collision operator, to model the reference experiment. Shown in Fig. 1(a), simulations are initiated by heating electrons with a radial profile $H(x,y) \propto \exp[-(x^2+y^2)/R_h^2]$ within a thin, dense target, producing an expanding plasma plume. All boundaries are periodic where the heated plume collides with itself along the inflow dimension (X), which is much shorter than the outflow (Y) and vertical (Z) dimensions. From the observed simulation ablation profiles, we measure n_{ab} and T_{ab}, the ablation density and temperature [32], where the heating operator magnitude is tuned to obtained the desired T_{ab}. We can then define the ablation ion skin depth, $d_{i0} = (M_i/n_{ab}Ze^2\mu_0)^{1/2}$, and the sound speed,
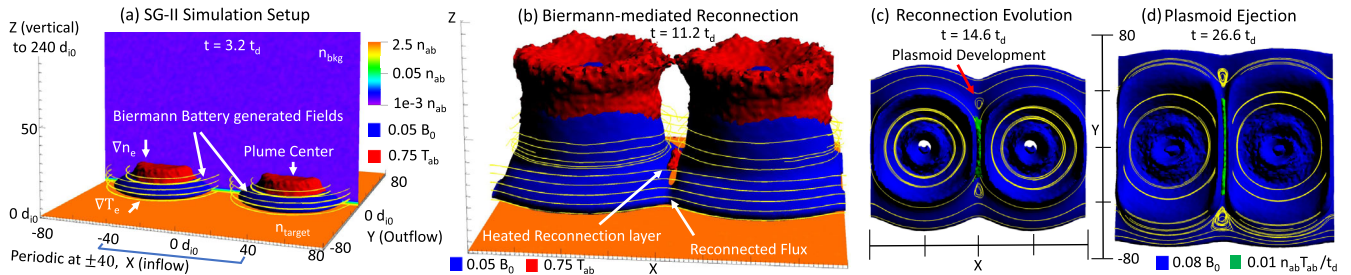

FIG. 1. Collision of self-magnetized plume with itself at four times, where two inflow (X) periods are shown. (a) Early time snapshot detailing setup of simulation; shown are two planar slices of n_e [one through the target $(z = 0 d_{i0})$ and one through the inflow, vertical plane $(XZ, y = 0 d_{i0})$], magnetic field lines in yellow, $|B|/B_0 = 0.05$ contour in blue, and $T_e/T_{ab} = 0.75$ contour in red. (b) Demonstration of Biermann-mediated reconnection at time $t = 11.2 t_d$. (c),(d) Top down views of later time field evolution $(t = 14.6 t_d$ and $26.6 t_d$, respectively), including plasmoid ejection and current sheet stretching—here the blue contour represents $|B|/B_0 = 0.08$, and green represents $E \cdot j/(en_{ab}T_{ab}/t_d) = 0.01$.

$C_{s,\mathrm{ab}} = (Zk_bT_{\mathrm{ab}}/M_i)^{1/2}$. Together these define the ablation timescale $t_d = d_{i0}/C_{s,\mathrm{ab}}$ and the characteristic magnetic field $B_0 = \sqrt{\mu_0 n_{\mathrm{ab}} k_b T_{\mathrm{ab}}}$. Normalizing our simulations to ablation units allows us to match PSC results to physical values of $n_{\mathrm{ab,phys}}$, $T_{\mathrm{ab,phys}}$, $d_{i0,\mathrm{phys}}$, and $t_{d,\mathrm{phys}}$ obtained from a similar analysis of radiation-hydrodynamic simulations performed with the DRACO code [33]. For reference, $n_{\mathrm{ab,phys}} = 3 \times 10^{27}$ m^{-3}, $T_{\mathrm{ab,phys}} = 2$ keV, $C_{\mathrm{ab,phys}} \approx 300$ km/s, and $B_{0,\mathrm{phys}} = 1300$ T. Reference [32] presents the SG-II experimental parameters and the full computational scheme for modeling heating, ablation, and matching to DRACO simulations. In contrast to Ref. [32], we extend our simulations from 2D (XZ) to 3D (XYZ), allowing reconnection.

We use a compressed electron-ion mass ratio, $Zm_e/M_i = 1/64$, ($Z = 1$) and a compressed ratio between T_{ab} and the electron rest mass energy $T_{\mathrm{ab}}/m_e c^2 = 0.04$. We compress these values far below the physical ratios while achieving convergence in our results, provided $Zm_e/M_i, T_{\mathrm{ab}}/m_e c^2 \ll 1$; in analogous 2D simulations, ratios down to $Zm_e/M_i = 1/400$ show convergence with $Zm_e/M_i = 1/64$. A box of $80 \times 160 \times 480 d_{i0}(L_x, L_y, L_z)$ is used, with the grid cell spacing $\Delta x < d_{e0}, 5\lambda_{D,\mathrm{ab}}$, where $\lambda_{D,\mathrm{ab}} = \sqrt{\epsilon_0 k_b T_{\mathrm{ab}}/n_{\mathrm{ab}} e^2}$. The SG-II heating radius $R_h/d_{i0} = 12$ with bubble separation $L_x/d_{i0} = 80$. Further parameters include the target width $= 2d_{i0}$, the target density $= 2.5n_{\mathrm{ab}}$, the background density $= 0.001n_{\mathrm{ab}}$, the target and background $T_e = 0.025\,T_{\mathrm{ab}}$, and 50 second-order-shaped particles are used per cell at n_{ab}. The collisionality, described by λ_{mfp}, the mean free path of electrons at T_{ab} and n_{ab}, is matched to the electron skin depth d_{e0} to preserve the correct collisional diffusivity of the magnetic field; $\lambda_{\mathrm{mfp}}/d_{e0} = 20$. While λ_{mfp} is resulting mismatched on d_{i0} scale, throughout the plume collision region we recover the correct collisionality regime, i.e., $\lambda_{\mathrm{mfp}} > \delta_{\mathrm{rec}}$, where δ_{rec} is the current sheet width.

Figures 1 and 2, respectively, show 3D snapshots and 2D profile slices of the SG-II magnetized plume collision. Figure 1(a) demonstrates the plume ablation, where the magnetic field is generated via $-(1/n_e e)\nabla n_e \times \nabla T_e$ due to the resulting density and temperature profiles, as demonstrated in Ref. [32]. By $t = 11.2t_d$, seen in Fig. 1(b), the

toroidal fields have collided and begun to reconnect. In Fig. 1(c), at $t = 14.6t_d$, we observe field energy conversion in the reconnection current sheet between the inflow fields ($\boldsymbol{E} \cdot \boldsymbol{j} > 0.01 n_{\mathrm{ab}} T_{\mathrm{ab}}/t_d$) and the development of closed-flux-surface plasmoidlike structures in the outflow. The associated inflow plane profiles at $t = 14.6t_d$ of n_e, T_e, J_z, and inflow field B_y are shown in Figs. 2(a)–2(d). From Figs. 2(c) and 2(d), we find the upstream field at the edge of the current sheet is compressed to $0.17\,B_0$, a factor of 1.5–$2\times$ the nominal generated field of $\approx 0.1B_0$. This observation is in contrast to 2D HED driven reconnection simulations, which find pileup ratios of $4\times$ the nominal inflow field [16]. In physical units, the observed compressed field corresponds to 220 T, comparable to the 370 T estimated in the experiment [7].

Figure 2(e) presents the downstream magnetic field in the outflow (YZ plane, $x = 0d_{i0}$) at $t = 14.6\,t_d$. For $z = 25$–$70\,d_{i0}$, moving in the $+y$ direction from the current sheet center at $y = 0\,d_{i0}$, we find B_x reverses its sign twice, around $y = 25\,d_{i0}$ and $y = 45\,d_{i0}$, where the first reversal corresponds to the center of the upper plasmoid in Fig. 1(c). Comparing Figs. 1(c) and 1(d), we find that the current sheet elongates as the plasmoids are ejected. Each plasmoid travels $\sim 20\,d_{i0}$ in $12\,t_d$, yielding an outflow speed of $1.66\,C_s \approx 500$ km/s, in agreement with the experiment, which observed plasmoids ejected in the outflow at 400 ± 50 km/s [6]. Discussed below, the creation and ejection of plasmoids appears to modulate the reconnection, particularly via the traceless pressure tensor. Biermann-mediated reconnection appears to be independent of plasmoid behavior.

Biermann-mediated reconnection.—The profiles shown in Figs. 1(b) and 2(a)–2(d) demonstrate how Biermann-mediated reconnection operates. The current sheet (around $x \approx 0d_{i0}$, $z \approx 20d_{i0}$) is relatively heated compared to both the inflow and outflow, as shown in Figs. 1 and 2(b). This local T_e maximum flips the direction of ∇T_e to point towards the plume collision center throughout the current sheet. Given ∇n remains directed toward the high-density target, $-(1/n_e e)\nabla n_e \times \nabla T_e$ in the current sheet destroys incoming flux (XZ plane) and generates reconnected flux in the outflow (YZ plane).
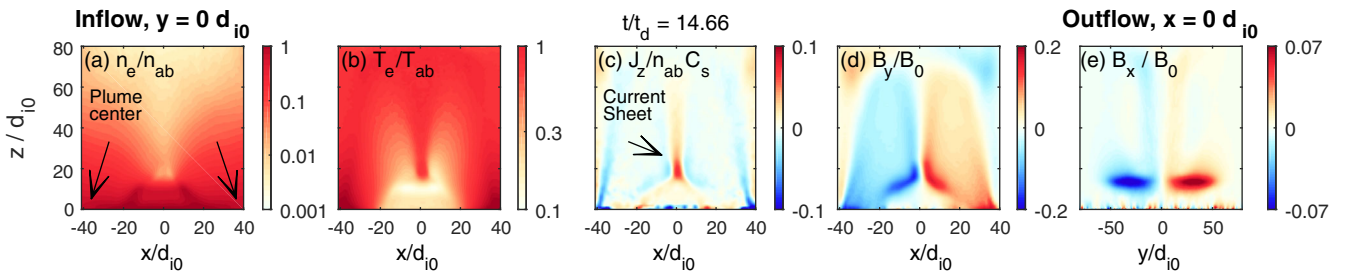

FIG. 2. (a)–(d) 2D slices along the inflow plane (XZ plane, $y = 0d_{i0}$) of n_e, T_e, J_z, and B_y at the SG-II scale at time $t = 14.6t_d$, where the bottom corners correspond to the center of the expanding plume and the dotted black line indicates the current sheet. (e) 2D slice along the outflow plane (YZ plane, $x = 0d_{i0}$) showing the downstream field B_x.
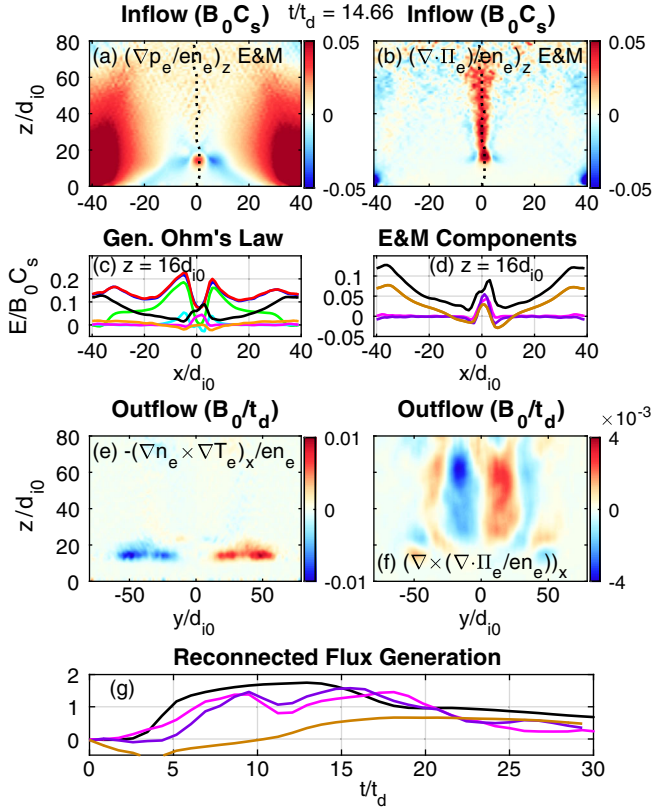
FIG. 3. (a),(b) 2D slice along the inflow plane of $(\nabla p_e/en_e)_{z,\text{em}}$ and $(\nabla \cdot \Pi_e/en_e)_{z,\text{em}}$, respectively; dotted black line indicates the current sheet, $(B_y/B_0 = 0)$. (c) Full out-of-plane generalized Ohm's law along the inflow at $y = 0d_{i0}$, $z = 16d_{i0}$: E_z in blue, sum of rhs of Eq. (1) in red, $v \times B$ in green, $-j \times B/n_e e$ in cyan, $\nabla p_e/en_e$ in black, $\nabla \cdot \Pi_e/en_e$ in magenta, and R_{ei}/en_e in orange. (d) Shows the same cut of full z component of $\nabla p_e/en_e$ and $\nabla \cdot \Pi_e/en_e$ (black and magenta, respectively) vs EM component of each term (brown and purple, respectively). (e),(f) The downstream flux creation in the outflow $(YZ, x = 0d_{i0})$ by $-(1/n_e e)\nabla n_e \times \nabla T_e$ and $-\nabla \times (\nabla \cdot \Pi_e/en_e)$, respectively. The quantities in (a)–(f) are calculated based on 2 d_{i0} averaging of plasma parameters in all three dimensions. (g) The rate of flux reconnection, $\dot{\Psi} = \int_C E_{z,\text{em}} dz$, where C is along the current sheet, by $(\nabla p_e/en_e)_{z,\text{em}}$ (brown) and $(\nabla \cdot \Pi_e/en_e)_{z,\text{em}}$ (purple). (g) Also shows $\dot{\Psi} = \int_0^{(L_z/2)} \int_0^{(L_y/2)} (\partial B_x/\partial t) dy dz$, the rate of flux creation in the outflow by Biermann, $-(1/n_e e)\nabla n_e \times \nabla T_e$ (black), and the traceless pressure tensor term, $-\nabla \times (\nabla \cdot \Pi_e/en_e)$ (magenta.)

In Fig. 3, we quantify the reconnection contribution of both the Biermann and traceless pressure tensor mechanisms. In 3D reconnection, the out-of-plane electric field E_z can have an electrostatic contribution in the current sheet that does not contribute to B-field evolution (i.e., reconnection.) Therefore, we extract the electromagnetic (EM) contribution of each term in Eq. (1) by solving for the divergenceless component of each rhs term via Fourier analysis. In Figs. 3(a) and 3(b), the electromagnetic

contributions to $E_{z,\text{em}}$ of the two mechanisms along the inflow (XZ) plane are presented, demonstrating $(\nabla p_e/en_e)_{\text{em}}$ contributes significantly to the reconnection E field in the current sheet (black dotted line) around $z \approx 16d_{i0}$, while $(\nabla \cdot \Pi_e/en_e)_{\text{em}}$ operates throughout the vertical current sheet. Figure 3(c) presents the full generalized Ohm's law for E_z at $z = 16d_{i0}$, showing strong ion inflow (green), Hall inflow (cyan), dissipation at $x = 0d_{i0}$ in the current sheet due to both $\nabla p_e/en_e$ (black) and $\nabla \cdot \Pi_e/en_e$ (magenta), and agreement between E_z and the sum of the rhs of Eq. (1) (blue and red, respectively). Figure 3(d) clarifies the dissipation terms, presenting both the full and EM contributions to Eq. (1). Comparing $\nabla p_e/en_e$ (black) vs $(\nabla p_e/en_e)_{z,\text{em}}$ (brown), we find the scalar pressure term has both significant electromagnetic and electrostatic components in the current sheet with $(\nabla p_e/en_e)_{z,\text{em}} = 0.03$ $B_0 C_s$. For the traceless pressure tensor term, we find $\nabla \cdot \Pi_e/en_e \approx (\nabla \cdot \Pi_e/en_e)_{z,\text{em}} = 0.055$ $B_0 C_s$. We define the local Alfvénic reconnection rate normalization as $B_{\text{up}}^* V_{A,\text{up}}^*$, where the maximum upstream field $B_{\text{up}}^* = 0.17$ B_0 and the Alfvén velocity $V_A^* = B_{\text{up}}^*/\sqrt{\mu_0 M_i n_i^*} = 0.85 C_s$, where $n_i^* = 0.04 n_{\text{ab}}$ is the current sheet ion density at $z = 16d_{i0}$. Noting $B_{\text{up}}^* V_{A,\text{up}}^* = 0.145 B_0 C_s$, we find the reconnection rate due to Biermann, $R_{\text{Biermann}} = (\nabla p_e/en_e)_{z,\text{em}}/B_{\text{up}}^* V_{A,\text{up}}^* \approx 0.2$ and $R_{\text{traceless}} = (\nabla \cdot \Pi_e/en_e)_{z,\text{em}}/B_{\text{up}}^* V_{A,\text{up}}^* \approx 0.38$. The local reconnection rate is the sum of these rates, yielding $R \approx 0.58$, which is the maximum rate observed in the simulation.

Figures 3(e) and 3(f) show the outflow $(YZ$ plane) B-field generation $((\partial B_x/\partial t))$ due to $-(1/n_e e)\nabla n_e \times \nabla T_e$, Biermann, and $-\nabla \times (\nabla \cdot \Pi_e/en_e)$, the traceless pressure tensor, where the latter appears to be associated with plasmoid formation from $z = 25$–80 d_{i0}. Figure 3(g) quantifies the full picture: the rate of total flux reconnection, calculated by $(\nabla p_e/en_e)_{\text{em}}$ and $(\nabla \cdot \Pi_e/en_e)_{\text{em}}$, vertically integrated along the current sheet (brown and purple, respectively) vs time, as well as the downstream flux generation rate by Biermann, as in Fig. 3(e), and the traceless pressure tensor, as in Fig. 3(f), integrated over the outflow (respectively shown in black and magenta.) For the traceless pressure tensor, the reconnected flux (purple) matches the flux creation downstream (magenta) at both scales, and we find global reconnection to speed up around $t = 14t_d$, corresponding to the plasmoid creation. Subsequently $(t = 17$–$30t_d)$, reconnection progressively slows as the plasmoids are ejected and the current sheet lengthens. For the Biermann term, we find reconnection (brown) does not match downstream flux generation (black), indicating that some downstream flux generation by the Biermann effect occurs separately from the reconnection. Biermann reconnection does not slow with current sheet elongation and ultimately constitutes $\approx 25\%$ of the total reconnection, whereas the Biermann term generates roughly 50% of the downstream flux.

Biermann reconnection rate.—To evaluate when the Biermann-battery effect should be considered in a reconnection scenario, we compare estimates of R_{Biermann} against the typical fast reconnection value of $0.1 B_{\text{up}} V_A$ [34]. The Biermann mechanism requires a heated reconnection layer T_e with an associated inflow scale length L_T, coupled with a significant out-of-plane n_e variation with scale length L_n. Considering $-(1/n_e e)\nabla n_e \times \nabla T_e$ operating over a reconnection layer width of δ_{rec}, the rate of flux destruction in the reconnection layer, normalized to $B_{\text{up}}^* V_A^*$, can be approximated as

$$R_{\text{Biermann}} \approx \frac{\delta_{\text{rec}} T_e}{e L_T L_n B_{\text{up}}^* V_A^*} = \frac{\beta_e}{2} \frac{\delta_{\text{rec}} d_{i,\text{rec}}}{L_T L_n}, \qquad (2)$$

where in the second equality we have substituted $\beta_e = n_e T_e/(B_{\text{up}}^{*2}/2\mu_0)$, and $d_{i,\text{rec}}$ as the local ion inertial length, demonstrating R_{Biermann} scales with reconnection layer β_e. In our simulations for $t = 14 t_d$, $z = 16 d_{i0}$, given $T_{e,\text{rec}} \approx T_{\text{ab}}$, $\beta_e \approx 2.8$, $L_T \approx 10 d_{i0}$, $\delta_{\text{rec}} \approx d_{i,\text{rec}} = 5 d_{i0}$, $L_n \approx 14 d_{i0}$, we find $R_{\text{Biermann}} \approx 0.25$, in agreement with results above.

From Ref. [27], we use R_{Biermann} to evaluate the possibility of Biermann-mediated reconnection within the turbulent magnetosheath. Referring to the current sheet parameters presented therein, we find $B_{\text{in}} \approx 20$ nT, $V_A \approx 200$ km/s, $T_{e,\text{rec}} \approx 100$ eV, $L_T \approx 180$ km, and $\delta_{\text{rec}} \approx 90$ km, and we estimate $L_n \approx 240$ km given associated density measurements. These estimates yield $R_{\text{Biermann}} \approx 0.05$, comparable to the observed normalized reconnection rate of 0.1, demonstrating that Biermann reconnection may play a significant role in this system [27].

The simulations presented in this Letter go beyond previous studies by capturing the full end-to-end 3D evolution, from self-consistent field generation to reconnection, of a recent MHD-scale HED reconnection experiment. We find general agreement in B-field generation and plasmoid dynamics between simulation and experiment, and detailed analysis of our results reveals that the Biermann-battery effect plays a direct role in the 3D fast magnetic reconnection. In addition to in HED regimes, we show using the dimensionless parameter R_{Biermann} that Biermann-mediated reconnection may play a role in turbulent 3D reconnection within the magnetosheath, which may be observed by the Magnetospheric Multiscale Mission. We further propose that this effect could be important in heliosheath and in mediating the initial fast reconnection necessary for large-scale dynamo.

---

*jmatteuc@pppl.gov

[1] L. Biermann, Z. Naturforsch **5A**, 65 (1950).

[2] R. M. Kulsrud, R. Cen, J. P. Ostriker, and D. Ryu, Astrophys. J. **480**, 481 (1997).

[3] P. M. Nilson, L. Willingale, M. C. Kaluza, C. Kamperidis, S. Minardi, M. S. Wei, P. Fernandes, M. Notley, S. Bandyopadhyay, M. Sherlock, R. J. Kingham, M. Tatarakis, Z. Najmudin, W. Rozmus, R. G. Evans, M. G. Haines, A. E. Dangor, and K. Krushelnick, Phys. Rev. Lett. **97**, 255001 (2006).

[4] C. K. Li, F. H. Séguin, J. A. Frenje, J. R. Rygg, R. D. Petrasso, R. P. J. Town, O. L. Landen, J. P. Knauer, and V. A. Smalyuk, Phys. Rev. Lett. **99**, 055001 (2007).

[5] L. Willingale, P. M. Nilson, M. C. Kaluza, A. E. Dangor, R. G. Evans, P. Fernandes, M. G. Haines, C. Kamperidis, R. J. Kingham, C. P. Ridgers, M. Sherlock, A. G. R. Thomas, M. S. Wei, Z. Najmudin, K. Krushelnick, S. Bandyopadhyay, M. Notley, S. Minardi, M. Tatarakis, and W. Rozmus, Phys. Plasmas **17**, 043104 (2010).

[6] J. Zhong, Y. Li, X. Wang, J. Wang, Q. Dong, C. Xiao, S. Wang, X. Liu, L. Zhang, L. An, F. Wang, J. Zhu, Y. Gu, X. He, G. Zhao, and J. Zhang, Nat. Phys. **6**, 984 (2010).

[7] Q. L. Dong *et al.*, Phys. Rev. Lett. **108**, 215001 (2012).

[8] M. J.-E. Manuel, C. K. Li, F. H. Séguin, J. Frenje, D. T. Casey, R. D. Petrasso, S. X. Hu, R. Betti, J. D. Hager, D. D. Meyerhofer, and V. A. Smalyuk, Phys. Rev. Lett. **108**, 255006 (2012).

[9] L. Gao, P. M. Nilson, I. V. Igumenschev, S. X. Hu, J. R. Davies, C. Stoeckl, M. G. Haines, D. H. Froula, R. Betti, and D. D. Meyerhofer, Phys. Rev. Lett. **109**, 115001 (2012).

[10] M. J. Rosenberg, C. K. Li, W. Fox, A. B. Zylstra, C. Stoeckl, F. H. Séguin, J. A. Frenje, and R. D. Petrasso, Phys. Rev. Lett. **114**, 205004 (2015).

[11] M. Yamada, R. Kulsrud, and H. Ji, Rev. Mod. Phys. **82**, 603 (2010).

[12] R. J. Hastie, Astrophys. Space Sci. **256**, 177 (1997).

[13] R. P. Lin and H. S. Hudson, Sol. Phys. **50**, 153 (1976).

[14] T. D. Phan, M. A. Shay, J. T. Gosling, M. Fujimoto, J. F. Drake, G. Paschmann, M. Oieroset, J. P. Eastwood, and V. Angelopoulos, Geophys. Res. Lett. **40**, 4475 (2013).

[15] G. Fiksel, W. Fox, A. Bhattacharjee, D. H. Barnak, P.-Y. Chang, K. Germaschewski, S. X. Hu, and P. M. Nilson, Phys. Rev. Lett. **113**, 105003 (2014).

[16] W. Fox, A. Bhattacharjee, and K. Germaschewski, Phys. Rev. Lett. **106**, 215003 (2011).

[17] W. Fox, A. Bhattacharjee, and K. Germaschewski, Phys. Plasmas **19**, 056309 (2012).

[18] A. S. Joglekar, A. G. R. Thomas, W. Fox, and A. Bhattacharjee, Phys. Rev. Lett. **112**, 105004 (2014).

[19] S. R. Totorica, T. Abel, and F. Fiuza, Phys. Rev. Lett. **116**, 095003 (2016).

[20] K. M. Schoeffler, N. F. Loureiro, R. A. Fonseca, and L. O. Silva, Phys. Rev. Lett. **112,** 175001 (2014).

[21] Y. L. Ping, J. Y. Zhong, Z. M. Sheng, X. G. Wang, B. Liu, Y. T. Li, X. Q. Yan, X. T. He, J. Zhang, and G. Zhao, Phys. Rev. E **89,** 031101 (2014).

[22] X. Wang, A. Bhattacharjee, and Z. W. Ma, J. Geophys. Res. **105,** 27633 (2000).

[23] W. Fox, F. Sciortino, A. v. Stechow, J. Jara-Almonte, J. Yoo, H. Ji, and M. Yamada, Phys. Rev. Lett. **118,** 125002 (2017).

[24] M. Hesse and D. Winske, J. Geophys. Res. **103,** 26479 (1998).

[25] J. R. Rygg, F. H. Séguin, C. K. Li, J. A. Frenje, M. J.-E. Manuel, R. D. Petrasso, R. Betti, J. A. Delettrez, O. V. Gotchev, J. P. Knauer *et al.*, Science **319,** 1223 (2008).

[26] C. K. Li, F. H. Séguin, J. A. Frenje, M. Rosenberg, R. D. Petrasso, P. A. Amendt, J. A. Koch, O. L. Landen, H. S. Park, H. F. Robey *et al.*, Science **327,** 1231 (2010).

[27] A. Retinò, D. Sundkvist, A. Vaivads, F. Mozer, M. André, and C. J. Owen, Nat. Phys. **3,** 235 (2007).

[28] M. Opher, J. F. Drake, M. Swisdak, K. M. Schoeffler, J. D. Richardson, R. B. Decker, and G. Toth, Astrophys. J. **734,** 71 (2011).

[29] Y. Matsumoto, T. Amano, T. N. Kato, and M. Hoshino, Science **347,** 974 (2015).

[30] E. S. Weibel, Phys. Rev. Lett. **2,** 83 (1959).

[31] K. Germaschewski, W. Fox, S. Abbott, N. Ahmadi, K. Maynard, L. Wang, H. Ruhl, and A. Bhattacharjee, J. Comput. Phys. **318,** 305 (2016).

[32] W. Fox, J. Matteucci, C. Moissard, D. B. Schaeffer, A. Bhattacharjee, K. Germaschewski, and S. X. Hu, arXiv: 1712.00152.

[33] S. X. Hu, D. T. Michel, D. H. Edgell, D. H. Froula, R. K. Follett, V. N. Goncharov, J. F. Myatt, S. Skupsky, and B. Yaakobi, Phys. Plasmas **20,** 032704 (2013).

[34] L. Comisso and A. Bhattacharjee, J. Plasma Phys. **82,** 595820601 (2016).